4
EXPERIMENTAL

This chapter covers the details of the material, welding processes, and characterization techniques used in the study. It includes the chemical composition of base and filler metals, welding procedures, and parameters. Various characterization techniques are discussed for examining structural integrity and structure-property relationships. The chapter also addresses residual stress measurement, along with an exploration of tribological and corrosion behavior.

4.1 MATERIALS AND WELDING PROCEDURE

The candidate materials selected for this experiment included super duplex stainless steel (sDSS 2507), Nickel-based superalloy (IN-625), Pipeline steel (X-70), and nitronic steel (N50). Plates with dimensions of 150 mm x 60 mm x 10 mm were extracted from the as-received material. The filler metals used comprised the sDSS-based ER2594, Ni-based superalloy ERNiCrMo-3, austenitic-based filler ER 309L, and carbon steel filler ER70S-2 (2.4 mm diameters). Table 4.1 depicts the findings of an optical emission spectrometer (OES) used to certify the composition of the base metals, filler wires, and weldments for all fillers. Therefore, the selection of ER2594, ER309L, and ERNiCrMo-3 as the overmatching consumables for joining sDSS 2507/IN-625, X-70, and N50, respectively, is due to their superior chemical compatibility with these base metals (BM). The plates were cut through wire-cut electrical discharge machining (WCEDM) before the welding to get a single V groove butt joint. As per the (Code-Steel & Structural Welding, 2010), each section was machined on the shaper to get a single V groove butt joint of 60º with a 2 mm root gap and root face, as shown in Figure 4.1(a). Subsequently, all the edges and abutting surfaces were cleaned chemically and mechanically to remove the contamination sources like rust, oil, moisture, and dirt that could sneak into the weld metal (WM) and cause weld defects afterward. To ensure excellent weldability and defect-free joint, abutting surfaces were cleaned thoroughly with a stainless-steel wire brush, followed by acetone swabbing. For the fitting-up of plates before filling the weld joint, tack welds with the same filler were performed at three locations to ensure the proper alignment of the joint. Subsequently, the root pass was done using the multi-pass gas tungsten arc welding (GTAW) process with the mentioned welding parameter. Welding parameters for filler metal selection and heat input investigation in sDSS 2507/N50 dissimilar weld joints (DWJs) are in Tables 4.2 and 4.3. Table 4.4 shows variable parameters for filler metal in sDSS 2507/IN-625 DWJs. For heat input effects in sDSS 2507/IN-625 and X-70 DWJs, welding parameters are in Table 4.5. Non-variable parameters for all weldments are tabulated in Table 4.6.

The multi-pass GTAW was operated manually with direct current electrode negative (DCEN) polarity in a flat (1G) position without weaving, as shown in Figure 4.1(b and c). For heat input calculation, utmost care was taken throughout arc recording on time to assist the welding speed. Among all the variables, as mentioned in Table 4.2-4.6, the welding current is the most significant variable, which influences the current density and, consequently, the melting rate of both base and filler metal. By keeping in mind these facts, two different combinations of heat input analogous to two different welding currents, i.e., 130/135A for lower heat input and 172/195 A for higher heat input, were selected for this experiment (arc efficiency = 60 % (Fujiyama et al., 2021)). The following equation. 4.1 describes the connection between welding parameters and heat input.

$$HI = \eta * \frac{V(voltage) \times I(welding\ current)}{S(welding\ speed)} \quad (4.1)$$

The GTAW process was employed to create a dissimilar welded joint, as illustrated in Figure 4.1(d and e). Visual inspections were conducted before and after welding, ensuring geometrical consistency and the absence of defects like blow holes or surface porosity. The schematic set-up of the GTAW process is depicted in Figure 4.2(a). The chromium and nickel equivalents (Cr_{eq} and Ni_{eq}) of the base and filler metals were measured using an equation. 4.2 and equation. 4.3 (W. N. Khan & Chhibber, 2021a) and tabulated in Table 4.1.

$$Cr_{eq} = Cr + 0.48Si + 1.5Mo + 1.5W + 1.75Nb + 2.3V + 2.5Al \quad (4.2)$$

$$Ni_{eq} = Ni + Co + 0.01Mn^2 + 0.1Mn + 18N + 30C \quad (4.3)$$

Table 4.1 : Chemical composition (wt. %) of the base metals and filler metals

Material	*Element (%wt.)*	*C*	*Mo*	*Ni*	*Si*	*Mn*	*Cr*	*Fe*	Cr_{eq}	Ni_{eq}
Base metals	sDSS 2507	0.03	3.90	7.03	0.50	0.75	25.03	Rem.	29.5	8.58
	IN-625	0.03	8.15	61.9	0.10	0.10	21.9	Rem.	38.2	63.2
	N50	0.04	2.30	12.1	0.48	4.98	21.4	Rem.	24.4	14.8
	X-70	0.06	0.001	0.35	0.46	0.85	0.006	Rem.	0.55	2.31
Filler metals	ER 2594	0.017	3.80	9.50	0.50	0.60	24.9	Rem.	30.8	12.7
	ER NiCrMo-3	0.012	9.82	64.1	0.10	0.38	20.8	Rem.	33.1	64.2
	ER 70S-2	0.04	0.005	0.02	0.82	1.40	0.04	Rem.	0.58	1.38
	ER 309L	0.03	0.17	13.5	0.56	1.80	23.1	Rem.	24.6	14.12

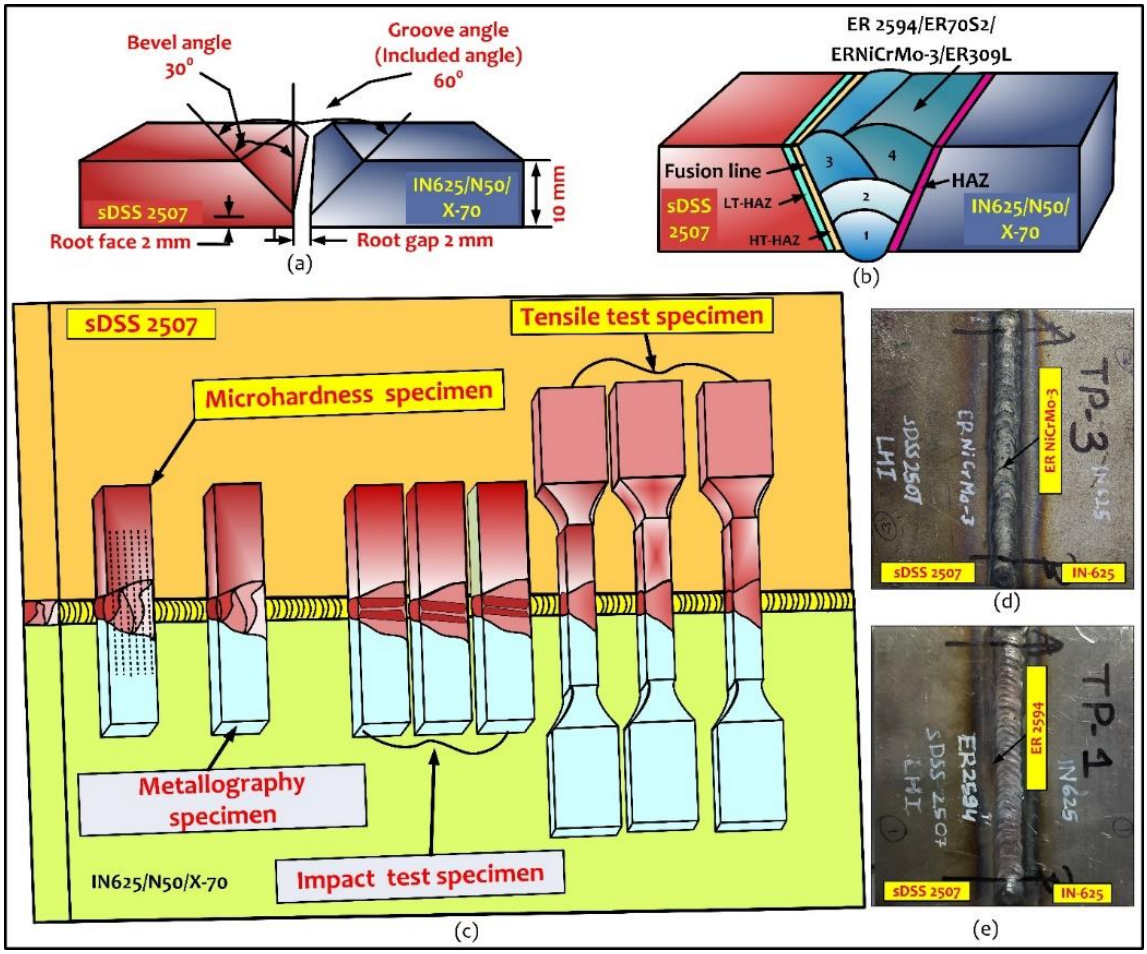


Figure 4.1 : Schematic diagram of (a) the V-groove geometry, (b) the sequence of passes and heterogeneity across the weldment during GTAW, (c) Schematic diagram of standard specimen extraction and its dimensions, (d and e) top view for ER2594 and ERNiCrMo-3 filler metal of the sDSS 2507 and IN-625 weldment, respectively

Table 4.2 : Variable parameters for filler metal selection of sDSS 2507/N-50 DWJs

Pass	*Arc Voltage (V)*	*Welding Current (A)*	*Welding Speed (mm/min)*	*Heat input (kJ/mm)*
Root	12	120	100	0.576
Filling	12	130	90	0.624
Capping	12	130	90	0.624
Backing	12	130	90	0.624

Table 4.3 : Variable parameters for heat-input weldment of sDSS 2507/N-50 DWJs

Sample	*Pass*	*Arc voltage (V)*	*Welding current (A)*	*Welding speed (mm/min)*	*Average heat input (kJ/mm)*	*Total heat input (kJ/mm)*
LHI	Root	14	150	90	0.84	2.712
	Filling	12	130		0.624	
	Capping	12	130		0.624	
	Backing	12	130		0.624	
HHI	Root	14	150	90	0.84	3.87
	Filling	16	172		1.01	
	Capping	16	172		1.01	
	Backing	16	172		1.01	

Table 4.4 : Variable parameters for filler metal selection of sDSS 2507/IN-625 DWJs

Filler metals	*Passes*	*Welding parameters*			*Average heat input per unit length per pass (kJ/mm)*	*Total heat input (kJ/mm)*
		Average welding speed (mm/min)	*Welding current (A)*	*Arc voltage (V)*		
ER2594/ ERNiCrMo-3	Root	85	150	14	0.889	2.876
	Filling	80	130	12	0.702	
	Capping	85	130	12	0.661	
	Backing	90	130	12	0.624	

Table 4.5 : Variable parameters for heat-input weldment of sDSS 2507/IN-625 and X-70 DWJs

Weldment	*Pass sequence*	*Welding parameters*			*Average heat input per unit length per pass (kJ/mm)*	*Total heat input (kJ/mm)*
		Arc voltage (V)	*Welding current (A)*	*Welding speed (mm/min)*		
LHI	Root Pass	14	150	90	0.84	2.98
	Filling Pass	12	135	80	0.729	
	Capping Pass	12	135	80	0.729	
	Backing Pass	12	135	85	0.686	
HHI	Root Pass	14	150	90	0.84	4.97
	Filling Pass	16	195	80	1.404	
	Capping Pass	16	195	80	1.404	
	Backing Pass	16	195	85	1.321	

Table 4.6 : Non-variable parameters for the sDSS 2507/IN-625, X-70, N50s multipass GTAW weldments

Welding parameter	*Selection*
Polarity	direct current electrode negative (DCEN)
Electrode	AWS EWTH-2 (98% W + 2% Th)
Shielding gas flow rate	15 l/min
Filler wire	ER 2594, ER NiCrMo-3, ER 70S-2, ER309L
Arc gap	3 mm
Groove design	Single V groove
Shielding gas with purity	Argon (99.995 % pure)
Welding position	1G

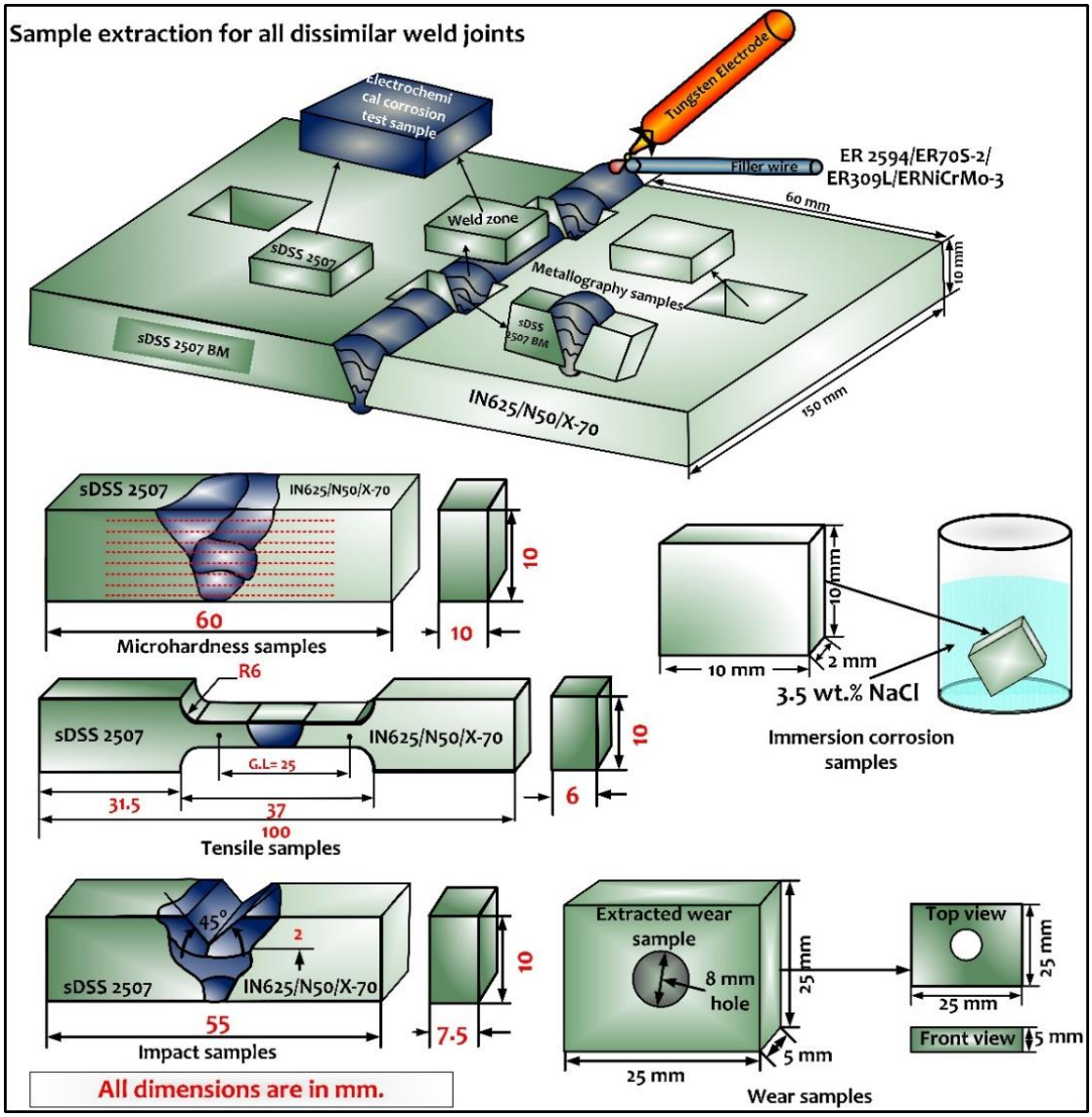


Figure 4.2 : The GTAW process schematic and extracted test specimen dimensions as per standards

4.2 METALLURGICAL CHARACTERIZATION

The weld joint specimens were cross-sectionally cut of dimensions 60 mm × 10 mm × 10 mm for the macrostructure and microstructure examination. The samples were then mechanically polished with emery paper of silicon carbide (220-2000 grit), trailed by disc polishing with a 1.5 µm diamond paste. Subsequently, a stereo zoom microscope was used to confirm the quality of weld beads with better geometrical shapes and showed the cross-section areas of the fusion and heat-affected zone (HAZ). American society for testing and materials (ASTM) E3-01 standard was followed for the polishing procedure for microstructural observations (Cotrim-Ferreira et al., 2010). The microstructure of the specimen was revealed by using etchants from Table 4.7, following the procedures set by ASTM E407-07. The macrostructure was investigated with the help of a stereo zoom microscope (Make: QUASMO, Model: SZB-45L). Macroscopically, the area of the cross sections was measured with the help of the Image J application. The microstructure of different zones like interfaces, HAZ, and weld metal employing different heat input conditions was investigated through an optical microscope (OM) and scanning electron microscope (SEM), and compositional analysis was studied through energy dispersive spectroscopy (EDS). X-ray diffraction was performed using a C_u K_α (λ = 0.154 nm)-equipped PANalytical X-ray diffractometer (XRD). In-depth electron probe microanalyzer (EPMA) investigations were performed on the weld joint's transition elements.

The weld zone (WZ) and polished weld interfaces were thinly sectioned and covered with a 30 nm thick carbon coating before EPMA research.

Table 4.7 : Etchants used to reveal the sDSS 2507/IN-625, X-70, N50s DWJ's microstructural characteristics

Etchant	*Methods/parameters*	*Composition*	*Application area*
Glyceregia	Swab method	10 ml HNO_3 + 20 ml glycerol + 30 ml HCL HNO_3	IN-625 base metal and interface
Nital (2%)	Swab method	2% HNO_3 + 98% C_2H_5OH	X-70 BM, ER 70S-2 weld zone
Modified Beraha II	voltage 5V, current density 1.1 A/cm^2, time 60 sec	20 ml HCl, 1.5g $K_2S_2O_5$, 0.7g $NH_4F.HF$, 80 ml water	For intermetallic phases
Electrolytically etching (10% oxalic acid)	voltage 9V, current density 1A/cm^2, time 40-60 sec	10g oxalic acid, 100 ml distilled water	sDSS 2507 base metal and ER 2594, ER 309L, and ERNiCrMo-3 weld zone

4.3 MECHANICAL CHARACTERIZATION

Mechanical tests were accomplished to investigate the mechanical properties of the sDSS 2507/IN-625, X-70, and N50 welded joints. To assess the tensile behavior, impact toughness values, and microhardness value of the welded joints, the specimens were cut according to the (ASTM American Society for Testing and Materials & ASTM E 23-12c, 2012; ASTM E8, 2010; ASTM E92-17, 2017), respectively. The transverse tensile tests were experimented on a universal testing machine (UTM) to ascertain the joint's strength, as schematically in Figure 4.2. The tensile specimens were subjected to a steady increment in axial load by setting the cross-head speed at 0.15 mm/min. The Vickers microhardness test was conducted to assess the microhardness of the same sample utilized for the metallographic analysis. Readings were taken in the transverse direction in accordance with (ASTM E92-17, 2017). Vickers microhardness measurement of the weld joint was accomplished in the transverse direction of the weldments by applying a 500 gm load with a holding time of 10 sec using a Vickers hardness tester. The microhardness measurement was performed on both weldments' base metal, heat-affected zone, and weld metal. To conduct the impact toughness test of the welded joint, the sub-sized Charpy impact test specimens with the dimensions of 55 mm x 10 mm x 7.5 mm (45º V-notches at the weld center) were extracted from both weldments. The fractured specimen of the tensile and impact test was analyzed by SEM equipped with EDS to assess fracture failure mode and compositional analysis of inclusion particles. Some samples from the base metal of tensile and impact tests were also conducted as a reference for comparison. All the mechanical tests were conducted at room temperature and were repeated thrice to check the repeatability of reported data. The mechanical properties of the tested base metals at room temperature are summarized in Table 4.8 for each material, according to the standards mentioned above.

Table 4.8 : Mechanical properties of the base metals and filler metals

Mechanical properties					
Base metal	*Tensile properties*			*Microhardness ($HV_{0.5}$)*	*Charpy toughness (J)*
	Tensile strength (MPa)	*Yield Strength (0.2% offset) (MPa)*	*Elongation (%)*		
sDSS 2507	1002 ± 3	910 ± 5	27 ± 2	310 ± 4	310 ± 5
IN-625	930 ± 5	500 ± 4	78 ± 3	260 ± 6	330 ± 7
N 50	915 ± 6	675 ±5	32 ± 5	315 ± 10	220 ± 5
X-70	612 ± 4	555 ± 4	30 ± 5	270 ± 5	292 ± 3

4.4 RESIDUAL STRESS MEASUREMENT

The deep hole drilling (DHD) strain gauge technique measured the residual stresses of the sDSS 2507/IN-625/X-70 DWJ using the GTAW process. The measurement was performed following the ASTM E837-13 standard's specifications (ASTM, 2001b). It is regarded as a method for estimating semi-destructive residual stresses, and in-plane biaxial residual stress fields can be found through thickness. Figure 4.3(a) depicts the measurement's location. The DHD technique consists of four fundamental steps, as shown in Figure 4.3(b)**.** In step 1, 3 mm-diameter reference holes were drilled through the thickness at the designated points. Later, an air probe was employed to gauge the reference holes' internal diameters ($d(\theta)$) in 1 mm increments along the thickness in both the longitudinal and transverse directions. After that, the internal diameters of the reference holes ($d'(\theta)$) were once again gauged through the thickness employing the air probe in the same locations as before. The magnitudes of in-plane residual stress were then determined using the diametral deformation $\left(\Delta d(\theta) = d'(\theta) - d(\theta)\right)$ of the reference hole consequent to various depth distances. Equation 4.4 below can be used to calculate the normalized strain ε (θ) connected with the residual stresses σ_x, σ_y, σ_{xy} and σ_z (Taraphdar et al., 2021)

$$\varepsilon(\theta) = \frac{\Delta d(\theta)}{d(\theta)} = -\frac{1}{E}\left[\sigma_x f(\theta) + \sigma_y g(\theta) + \sigma_{xy} h(\theta) - \mu\sigma_z\right] \quad (4.4)$$

Where $f(\theta) = 1 + 2\cos 2\theta$, $g(\theta) = 1 - 2\cos 2\theta$, $h(\theta) = 4\sin 2\theta$, E stands for Young's modulus, and υ stands for the Poison's ratio (Timoshenko & Goodier, 1951). The x-axis in the equation above has an angular orientation of $\theta = 0°$. It was assumed that there was no stress because of the value of σ_z. Equation 4.5 can be rewritten as follows:

$$\varepsilon(\theta) = \frac{\Delta d(\theta)}{d(\theta)} = -\frac{1}{E}\left[\sigma_x f(\theta) + \sigma_y g(\theta) + \sigma_{xy} h(\theta)\right] \quad (4.5)$$

Determine the magnitudes of longitudinal and transverse residual stresses by modifying Equation 5 to incorporate longitudinal (ε_x) and transverse (ε_y) strains by introducing θ = 0° and θ = 90°, as shown in equations 4.6 and 4.7.

$$\varepsilon_x = \frac{\Delta d_x}{d_x} = -\frac{1}{E}\left[3\sigma_x - \sigma_y\right] \quad (4.6)$$

$$\varepsilon_y = \frac{\Delta d_y}{d_y} = -\frac{1}{E}\left[3\sigma_y - \sigma_x\right] \tag{4.7}$$

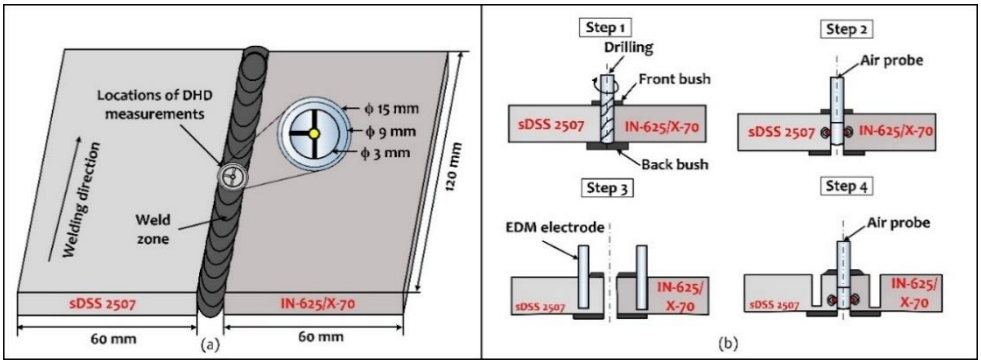


Figure 4.3 : (a) Locations of DHD measurements, (b) The steps involved in measuring residual stress using the DHD method (Dak & Pandey, 2021a)

4.5 TRIBOLOGICAL INVESTIGATIONS

The study seeks to provide insights that can be used for material selection, optimum heat input for weld fabrication, design optimization of sub-sea manifolds in slurry environments to achieve superior wear resistance and to aid in a deeper understanding of the slurry erosion behavior of the sDSS 2507/IN-625/X-70/N50 DWJs by identifying the primary mechanisms of wear and material loss.

4.5.1 SLURRY POT EROSION WEAR TEST

The slurry erosion wear tests were conducted using a Ducom TR-40 slurry erosion pot tester. Testing was conducted on 25 mm x 25 mm x 5 mm specimens with an 8 mm metallographically polished center hole. Figure 4.4 shows the slurry erosion pot tester schematic. Sieve analysis determined sand particle size distribution. Sand particles typically range from 100 µm to 600 µm in size. Sand particle SEM micrographs before erosion testing are presented in Figure 4.5(a). Spherical sand has a few sharp edges. Figure 4.5(b) shows the experiment sand particle size distribution. A material's susceptibility to slurry erosion depends on a number of factors, including particle size, impact angle, slurry concentration, particle shape, and impact velocity. The framework, six-station slurry vessel, motor, control system, and hollow rectangular cooling tank were used for slurry erosion testing. Adding varying volumes of sand to 600 mL of water produced slurries with different concentrations. The investigation employed slurries with 100-600 µm typical particle sizes and 10%-30% weight concentrations. Higher concentrations were employed to simulate severe slurry transportation. Each specimen was erosion-tested for 60 minutes at 400 rpm with fresh slurry. The erosion test measured material loss by comparing the test specimen's original and final weights. We used an electronic microbalance with a minimum count of ±0.0001 gram to measure weight change. The test sample was cleaned with acetone and dried in hot air before each cycle for accurate weight loss measurements. After slurry pot testing, the specimens' worn surfaces were evaluated under optical and scanning electron microscopes. The quantification and comparison of erosion rate are conducted by analyzing multiple factors, employing a methodology similar to that described by (Tarodiya & Gandhi, 2019), which involves calculating the average weight losses of the samples. Variables such as the exposed area of the specimen, the weight loss, the sand particle density, the solid concentration, the orientation angle, and the peripheral velocity of the worn samples all factor into the equation for the wear rate due to slurry erosion (Equation. 4.8). The weight concentration of slurry was converted to a volume concentration using a standard relationship given by (De Bree et al., 1982), as shown in equation 4.9.

$$E_w = \frac{W_{loss}}{\rho_s \times C_v \times A_{SP} \times T \times V_{SP} \times \sin\alpha} \quad (4.8)$$

$$C_v = \frac{C_w}{\rho_s - (\rho_s - 1) \times C_w} \quad (4.9)$$

Where: E_w is slurry erosion wear rate (g/g of solids), W_{loss} is average weight loss (g), ρ_s is the mass density of sand particles (kg/m^3), T is the testing time (s), $C_{v,} and\ C_w$ are solid concentration by volume and weight (fractions), respectively, V_{SP} is the peripheral velocity of the specimen (m/s), A_{SP} is exposed surface area (m^2), $and\ \alpha$ is orientation angle (°).

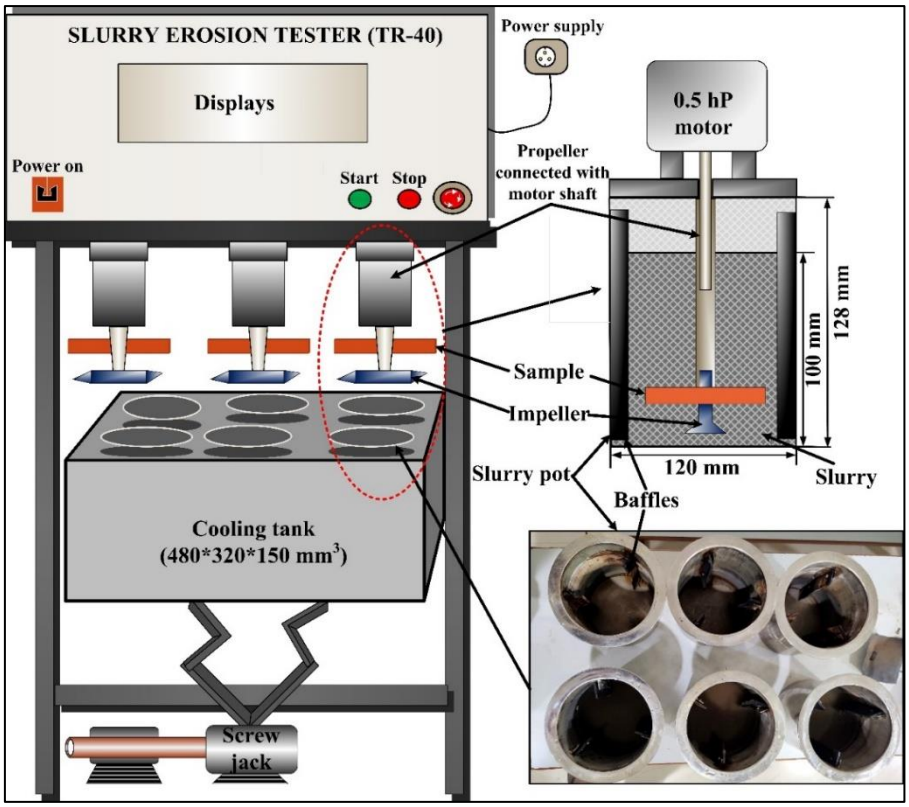
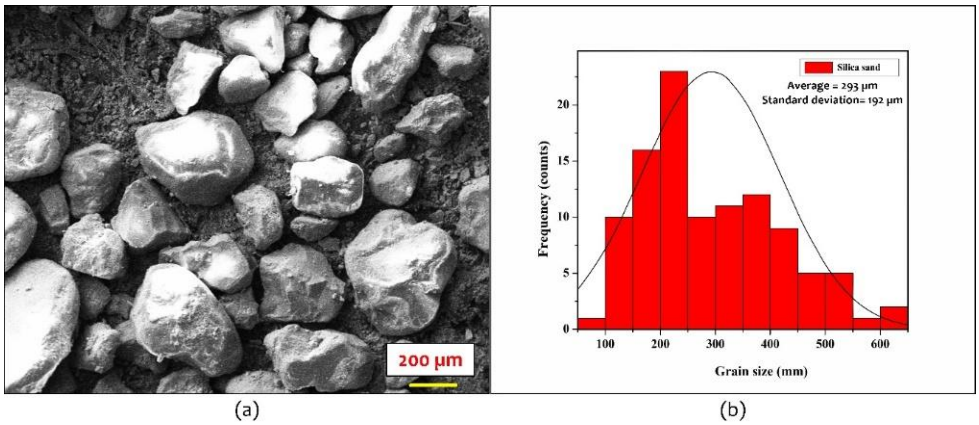


Figure 4.4 : Schematic illustration of the erosion experimental test rig



(a) (b)

Figure 4.5 : Representation of (a) SEM image of Silica sand and (b) average particle size distribution

4.5.2 PIN-ON-DISC WEAR TEST

A pin-on-disc tribometer with an 8 mm base metal pin and both fillers' weld zones studied dry wear behavior. Pin-on-disc tribometer schematics are presented in Figure 4.6. The EN-31 disk with obvious wear tracks is also schematically depicted in Figure 4.6. The disc was

cleaned with 220-grade emery paper after each experiment. Table 4.9 lists pin-on-disc tribometer test parameters. The base metal and weld zone wear tests involved rolling the cylindrical pin against a spinning counter face disc under 30 N (ASTM, 2000). The spinning speed was tuned to achieve 500–3000 m sliding distance. Before each test, acetone and 400-grit emery paper were used to clean the pin and maintain maximum pin-disc contact. Pins were weighed using an electronic scale with a ±0.1 mg resolution after each test. Weight loss due to wear was used to calculate cumulative volume loss and wear rate using the Archard equation. As the pin passes over the disc, its wear surface varies rapidly, as shown on the wear track profile, including size and form. Stereomicroscope observation examined these variations. The relationship between material hardness and wear resistance is well recognized, with harder materials typically exhibiting higher wear resistance. In addition to wear volume and weight loss, the pin's contact face profile and geometrical data have been studied to determine the progressive wear mechanism. The pin's worn surface was investigated using SEM to establish the wear process. Laboratory wear testing and tribological performance must be correlated due to multiple wear variables. Material, surface shape, and wear process factors affect wear resistance and friction coefficient. Analysis of wear test data is often performed using Archard's equation. This equation's wear test method and computations are explained by (Bressan et al., 2008). Equations 4.10-4.13 show that the equation can be used to calculate wear performance and wear test parameters.

$$Q(mm^3) = \frac{V}{S} = \frac{KF_N}{H} \tag{4.10}$$

$$K = \frac{QH}{F_N} = K_S H \tag{4.11}$$

$$K_S = \frac{Q}{F_N} \tag{4.12}$$

$$V = \frac{\Delta m}{\rho} \tag{4.13}$$

Archard's equation uses various parameters to compute the wear rate (Q), including the cumulative volume loss (V) in mm^3, the sliding distance (S) in meters, the applied normal load (F_N) in the unit of N, and the hardness (H) of the softer material (either the pin or the disc). The equation can also be used to calculate the wear coefficient (K) and the specific wear coefficient (Ks). The cumulative lost volume (V) in Equation 4.10 is an important factor in wear testing and is measured at the lab level by measuring the sliding pin's change in weight, Δm, in grams, and the material density, ρ, in g/cm^3. The wear coefficient K and other factors from the Archard wear equation describe wear severity.

Table 4.9 : Variable and constant parameters for the dry sliding wear test

Parameters	*Value/Descriptions*
Pin dimension	8 mm diameter and 20 mm length
Disc material	EN-31
Normal Load (N)	30 (Constant)
Track diameter (D)	55 mm
Sliding time (t)	15 min (Constant)
Sliding distances (m)	500, 1000, 1500, 2000, 2500, 3000
Rotational speed (rpm)	193, 386, 579, 772, 965, 1158

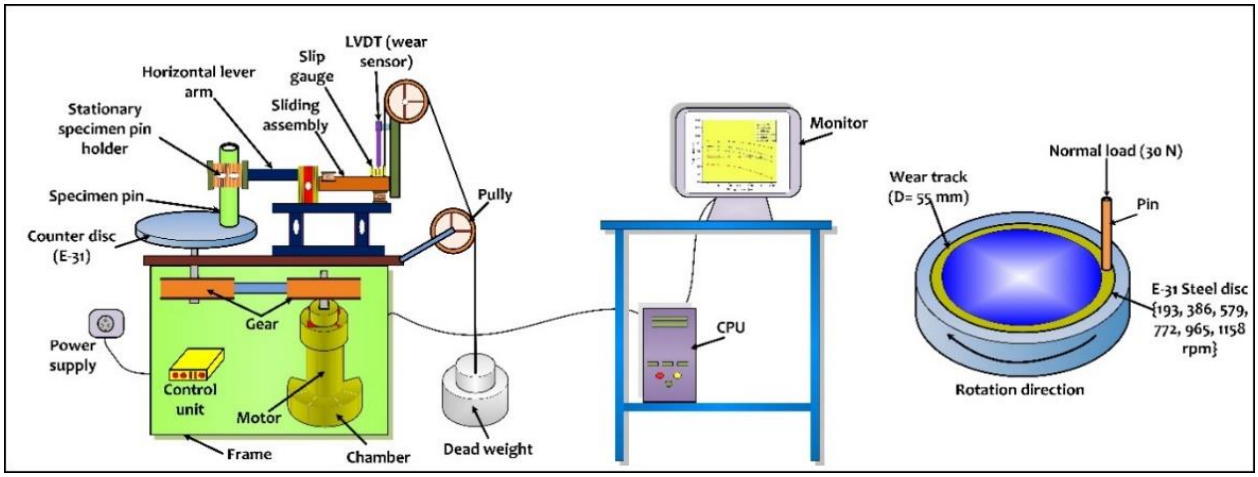


Figure 4.6 : Schematic of Pin-on disc tribometer experimental set-up and EN-31steel disc with visible wear track

4.6 CORROSION INVESTIGATIONS

All the selected base materials have been considered corrosion-resistant alloys that can withstand harsh corrosive conditions, making this study essential for marine engineering and service applications, particularly for developing high-strength steel structures that can be used in hazardous marine environments. The study monitors weld metal and base metal precipitation and its impact on corrosion to maintain the structural integrity of the sDSS2507/IN-625/X-70/N50 DWJs.

4.6.1 ELECTROCHEMICAL MEASUREMENT

Corrosion has been quantitatively evaluated using a variety of electrochemical methods, such as Tafel plot analysis, open circuit potential (OCP), and electrochemical impedance spectroscopy (EIS). Tested welded samples for corrosion performance using EIS and potentiodynamic polarization in 3.5 wt.% NaCl solution at 25 ± 1 °C, following (ASTM, 2011) standards. Figure 4.7(a) shows the weldment sample extraction position of BM and weld zone corrosion specimens. Sample 4 has only WZ, while 1 and 5 have base metals. Samples 2 and 3 contain WZ, HAZ, and BM. Before testing, specimens 2 and 3 were etched and optically inspected for microzone homogeneity. Wire-cut electric discharge machining (WCEDM) was used to extract 10 × 5 × 0.5 mm^3 samples with a 5 mm^2 exposed surface. Before testing, the coupons were polished with 2000-grit emery paper, acetone-cleaned, distilled water-rinsed, and air-dried. An AUTOLAB three-electrode cell electrochemical workstation measured electrochemical data. A platinum rod was the counter electrode, an Ag/AgCl electrode was the reference electrode, and the specimen was the working electrode (Figure 4.7(b)). All potentials were reported using Ag/AgCl. All samples were stabilized for 30 minutes before electrochemical testing. A potential scanning rate of 0.1 mV/s was used for potentiodynamic polarization tests as per (ASTM, 2001a) standards. The potential range, including the transpassive zone, was -0.5 V to +0.5 V relative to OCP to compare weld metal localized corrosion resistance. EIS was performed from 100 kHz to 10 MHz following (ASTM, 2015) procedures with a 10-mV sinusoidal voltage signal amplitude. Nova 2.1.5 analyzed and fitted EIS data to generate an analogous circuit. Corroded specimen was evaluated three times after cyclic potentiodynamic polarization tests at 25 °C for repeatability. Tafel plot analysis is a common electrochemical technique that measures metal sample current by applying a potential scan up to ±25 mV around the open circuit voltage. The current is linear with voltage in this voltage range, and the slope shows polarization resistance (R_p). Polarisation resistance indicates an external potential's capacity to inhibit metal oxidation. Anodic (β_a) and cathodic (β_c) Tafel slopes (Equation 4.14) from linear polarization measurements can be used to calculate the corrosion rate, which is inversely proportional to R_p. The corrosion rate (mm/year) is calculated using Equation 4.15 (Zaveri et al., 2008).

$$I_{corr} = \frac{\beta_a \times \beta_c}{2.3R_P(\beta_a + \beta_c)} \quad (4.14)$$

$$CR(mm/year) = \frac{I_{corr}(A) \times K \times E.W(g/equivalent)}{A(cm^2) \times D(g/cm^3)} \quad (4.15)$$

4.6.2 IMMERSION CORROSION TESTS

The corrosion behavior of the sDSS 2507/ IN-625/X-70/N50 DWJs was examined using two immersion methods. Test coupons were ground and polished. Two coupons were tested for corrosion using weight loss and corrosion product analysis. Group A was exposed to a dry/wet cyclic environment, with alternately wet (24 hours at 25°C) and dry (24 hours at 25°C, 55% relative humidity (RH)) periods. In contrast, Group B was completely immersed in 3.5 wt.% NaCl. Measurement of the coupon weight was done before the corrosion test. Mixing deionized water with 3.5 wt.% NaCl simulated neutral seawater at pH 7.1. In Figure 4.7(c), coupons were put against a 200 mL beaker wall. Three samples of base metal and weld metal were tested at six different exposure times (3, 7, 14, 20, 30, 40, 50, and 60 days). A Labtronics automatic pH meter (LT-501) measured pH before and after each cycle, and the solution was replenished. After exposure, samples were rinsed with deionized water, dried, and inspected for surface quality with a Leica macroscope. Next, the samples were gently brushed to eliminate corrosion products. Table 4.10 describes the cleaning solutions used to visibly eliminate corrosion products from the affected regions (ASTM, 2004). Average weight loss was calculated using mean values after carefully measuring samples. All experimental conditions were repeated three times to ensure accuracy and reliability. After removing corrosion products, the weight, original weight, and exposed area of each sample were compared to estimate the average corrosion rate (CR, mm/year) for various corrosion periods. Equation 4.16 was used to calculate the corrosion rate in millimeters per year using weight loss in grams, sample external area in square centimeters, steel physical density, and corrosion time in hours (ASTM, 2004). Weight loss was used to assess corrosion dynamics after each corrosion cycle (Equation 4.16). Weight loss and initial total exterior area were used to assess dry/wet corrosion damage. Cross-sectioning corrosion samples revealed layer shape, scale structure, and thickness. The microstructures, compositions, and morphologies of corrosion products were studied using SEM with EDS.

$$CR\ (mm/year) = \frac{K \times W}{A \times T \times D} \quad (4.16)$$

In this instance, K represents a constant factor (8.76×10^{-4}) applied to evaluate the corrosion rate in millimeters per year. W is the sample's weight lost in grams. A represents the exposed surface area of the sample, measured in centimeter square. D stands for the tested steel's actual density. T is the corrosion's time scale, expressed in hours.

Table 4.10 : Details of cleaning solution utilized to remove inner corrosion products

Specimens	*Solutions*	*Time (min)*	*Temperature (°C)*
sDSS 2507 BM/sDSS 2507 weld interface and ER2594 /ER309L WZ	100 mL nitric acid, 20 mL hydrofluoric acid, Reagent water to make 1000 mL	5 to 20 min	20-25 °C
X-70 BM/ X-70 weld interfaces for both filler	500 mL hydrochloric acid, 3.5 g hexamethylene tetramine, Reagent water to make 1000 mL	10 min	20-25 °C
IN-625 BM and ERNiCrMo-3 WZ, IN-625 weld interface	150 mL hydrochloric acid, Reagent water to make 1000 mL	1 to 3 min	20-25 °C

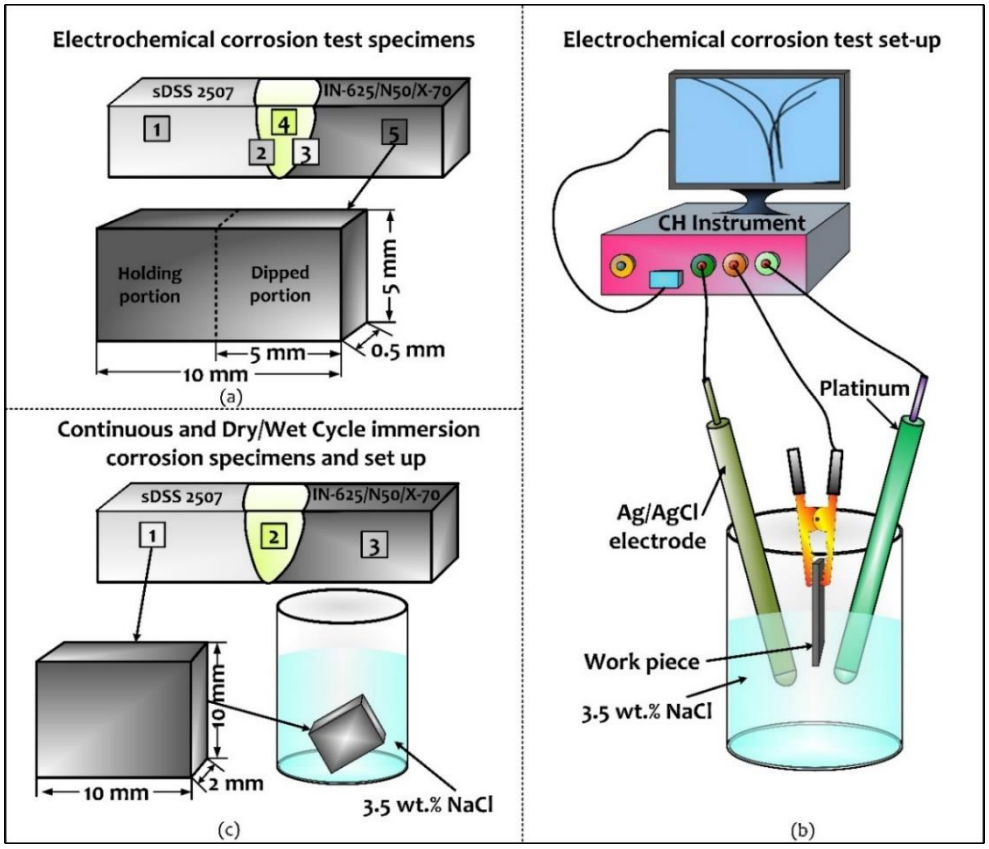


Figure 4.7 : Schematic details of specimen details and corrosion set-up of (a and b) electrochemical corrosion test, (c) immersion corrosion test

SUMMARY OF CHAPTER 4:

This chapter provides a comprehensive overview of the experimental methods employed in the study, covering material details, welding processes, and characterization techniques. It includes the chemical composition of base and filler metals, welding parameters, and extracted testing specimen adherence to ASTM standards for each test. The chapter discusses various characterization techniques for investigating structural integrity and structure-property relationships, including residual stress measurement, tribological, and corrosion behavior. While offering brief information on welding parameters, it sets the stage for more detailed exploration in Chapter 5, where the results and conclusions from the experiments will be thoroughly discussed.

....